Effect of initial damage on rock pulverization along faults

Mai-Linh Doan*, Virginie d'Hour

ISTerre, CNRS, Université Joseph Fourier, BP53, 38041 Grenoble Cedex 9, France

ARTICLE INFO

ABSTRACT

Pulverized rocks have been found in the damage zone around the San Andreas Fault, at distances greater than 100 m from the fault core. This damage is atypical in that it is pervasive and strain is not localized along main fractures as expected at these distances from the fault core. With high strain rate experiments, the authors have previously shown that above a strain rate threshold, the localization of strain along a few fractures is inhibited. Pulverized rocks may be generated by seismic waves at high frequency. Here we generalize these conclusions by discussing the effect of the initial fracture network in the sample on the transition from strain localization along a few fractures to diffuse damage throughout the sample. Experimental data are compared with statistical theory for fracture propagation. This analysis shows that the threshold in strain rate is a power law of initial fracture density and that a pre-damaged rock is easier to pulverize. This implies that pulverized rocks observed on the field may result from successive loadings.

© 2012 Elsevier Ltd. All rights reserved.

1. Introduction

Pulverized rocks have been observed near the San Andreas Fault (Wilson et al., 2005; Dor et al., 2006, 2009), and other large strike slip faults: Garlock Fault (Rockwell et al., 2009), Northern Anatolian Fault (Dor et al., 2008), and Arima-Takatsuki Fault (Mitchell et al., 2011). These rocks are found in outcrops of pervasively damaged rocks, which are sometimes as wide as several hundreds of meters. Due to the intense fracturing, individual samples typically crumble into powder when compressed by hand. Rockwell et al. (2009) have shown that the samples are microfractured, resulting in angular fragments about 100 μm in size. These rocks are only moderately chemically altered, so that their weakness cannot be attributed to weathering. High strain is one mechanism to explain the multiplicity of fractures: energy input rate is so high that it could not be accommodated by only a few fractures. A key observation is that the extensive damage of pulverized rocks is associated with small overall strain (Fig. 1). A second explanation for the diffuse damage pattern is high strain rate. With a higher energy supply rate, a single fracture with limited propagation speed cannot accommodate all of the applied energy. At higher strain rate, the finite velocity of stress waves also limits the expansion of the stress shadow zone around a major fracture, and interaction between fractures differs from the low strain rate case (Grady and Kipp, 1989; Hild et al., 2003b).

Pulverized rocks are localized within a few kilometers of the fault, with damage typically increasing closer to the fault core (Mitchell et al., 2011). This suggests that pulverization is related to fault activity. The origin of pulverized rocks is still debated, but most theories assume they are related to coseismic damage. The rarity of pulverization suggests that it is induced by an exceptional event, either by the tensile pulse predicted for rupture along bimaterial interfaces (Andrews and Ben-Zion, 1995), or by the Mach cone of a supershear rupture (Doan and Gary, 2009). Doan and Gary (2009) have shown experimentally that high strain rate loading can generate features similar to pulverization. They used samples from the Lake Hughes area of the Mojave segment of the San Andreas Fault (SAF), about 150 m away from the fault core. As a result of the proximity of the samples to the fault their experimental samples were pre-damaged.

The experiments reported here were conducted in a similar manner; a single, sudden and high energy loading event. Yet, thin sections of natural pulverized rocks reveal sealed microfractures (Fig. 1b), suggesting that the damage may be cumulative, and related to multiple loadings. These observations lead to the question: What is the effect of initial damage on the pulverization properties of rocks? In this paper, we investigate experimentally the effect of initial damage on the fragmentation process. We couple experimental results made on both pre-damaged and intact samples with the theory of Hild and Denoual (Hild et al., 2003a, 2003b; Denoual and Hild, 2000, 2002) to show that the threshold to pulverization decreases with greater initial damage. Hence, as

---

* Corresponding author. Tel.: +33 4 76 63 52 09; fax: +33 4 76 63 52 52.
  E-mail address: Mai-Linh.Doan@obs.ujf-grenoble.fr (M.-L. Doan).
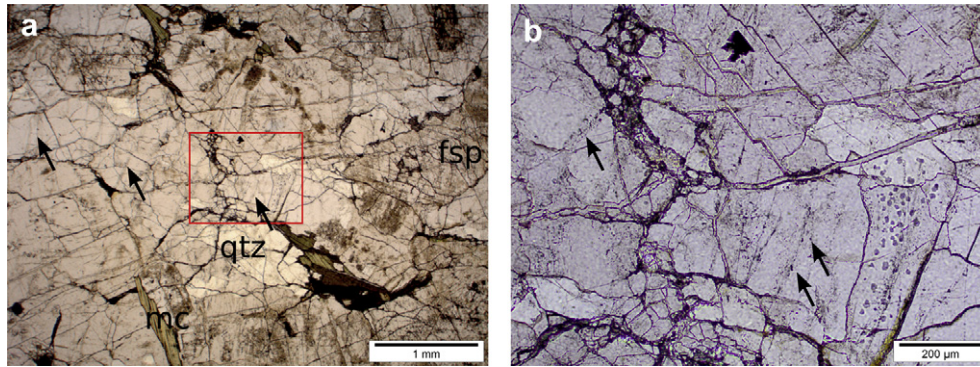
Fig. 1. (a) Thin section of a pulverized rock sampled near Mount Emma Road outcrop, located east of Palmdale, CA, along the Mojave segment of the San Andreas Fault (see also Fig. 3). Thin section was taken in plane polarized light. The outcrop location and description can be found in Fig. 1 of (Dor et al., 2006). Note the dense fracture network crosscutting grains and the preserved interlocked structure of the crystalline rock. The rock is severely damaged but with little shear displacement. Quartz (qtz) and feldspar (fsp) are affected, but the long, weak mica grain (mc) is only cleaved. (b) Zoom within the red rectangle of picture (a). Some sealed microfractures are highlighted by a series of fluid inclusions (black arrows), suggesting that the sample was previously damaged and healed (For interpretation of the references to color in this figure legend, the reader is referred to the web version of this article.).

rocks close to the fault get more and more damaged by successive loadings, pulverization becomes easier.

2. Experimental pulverization of rocks

2.1. Split Hopkinson pressure bars

When performing high strain rate testing, wave propagation time may not be negligible and the deformation measured at an individual strain gage may not be representative of the sample deformation Nemat-Nasser (2000). Moreover, classical servo-hydraulic machines have a limited loading velocity range leading to the use of Split Hopkinson Pressure Bars (SHPB) when applying strain rates above 100/s (Nemat-Nasser, 2000). In this study, we induce damage experimentally on protolith samples collected near the pulverized zone of the San Andreas Fault. The samples were loaded uniaxially at strain rate above 50/s, using the SHPB apparatus (Kolsky, 1963) at the Laboratoire de Mécanique des Solides of the École Polytechnique, Palaiseau, France.

Pulverized rocks have thus far only been documented in surface outcrops (Wilson et al., 2005; Dor et al., 2006, 2009, 2008; Mitchell et al., 2011) or in shallow boreholes at depths ¡50 m (Wechsler et al., 2011). The shallow borehole drilled along the San Andreas Fault provided samples free from surface alteration, that helped evaluate the relative timing of pulverization and surface alteration: Wechsler et al. (2011) argued that pulverization of outcrop rocks along the San Andreas Fault occurred recently, *i.e.* when the samples were at shallow depths. Therefore, we assume that unconfined conditions in our experiments are relevant for understanding rock pulverization, at least along the San Andreas Fault.

Each cylindrical sample is inserted between 2 bars and impacted by a striker bar arriving with a known speed (Fig. 2). The incident stress wave splits into reflected and transmitted waves when it reaches the sample. The incident and reflected waves are then measured with strain gages on the input bar and output bar.

Classical processing of the SHPB assumes 1-D propagation of elastic waves, given the dimensions of the bars (3 m in length by 4 cm in diameter). Here, we have taken into account the dispersion and attenuation processes predicted by the 3D-model of Pochhammer and Chree (Graf, 1991). Due to our sampling rate of 1 MHz, we could reconstruct precisely forces and displacements at both ends of the specimen. We checked that the forces were identical at the input and output bars to verify that the sample was homogeneously loaded. Once the quasi-equilibrium of the specimen is verified (equality of input and output forces), we calculated the history of stress, strain, and strain rate.

To ensure that the samples were loaded only once, the output bar is shorter than the input bar. Its exit extremity is free to move, allowing the output bar to move away from the sample before any reloading of the sample.

Experiments were conducted with strikers of various lengths (1.20 m, 0.9 m and 0.5 m), and with or without a lead foil inserted at the entry extremity of the input bar, which acts as a pulse shaper. By conducting experiments both with and without the pulse shaper we could decouple strain and strain rate.

2.2. Experiments done on samples from the damage zone of the San Andreas Fault

In this section, we briefly review the experiments (Doan and Gary, 2009) conducted on samples taken from near the San Andreas Fault, at the Lake Hughes outcrop. This outcrop has been described extensively in (Dor et al., 2006) (see their Figs. 1 and 5). Lying west of Palmdale city, CA, this outcrop is located in a narrow valley following the Mojave Segment of the San Andreas Fault. Although the fault itself is not visible, the damage zones of both sides of the fault are visible. The granite of the northern side is severely pulverized, with the intensity of pulverization decreasing rapidly (Fig. 3). The carbonate outcrop on the southern side is much less damaged. Samples were collected about 150 m from the fault core and were derived from the same protolith as the pulverized rocks but not pulverized themselves. The lithology of the samples is described in Table 1. We used this rock material to approximate the initial state before pulverization.

All samples have similar dimensions, 2.5 cm in diameter and 2.5 cm in length. The 1:1 aspect ratio offers a suitable compromise to minimize both stress shadow from sample ends (Paterson and Wong, 2005) and heterogeneity of stress in a long sample when the wave passes (Gama et al., 2004).
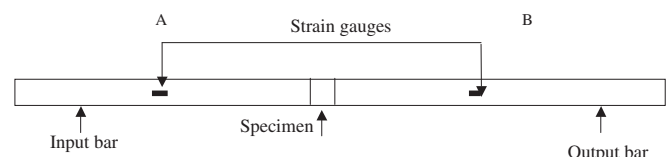
**Fig. 2.** Schematics of the split Hopkinson pressure bars.
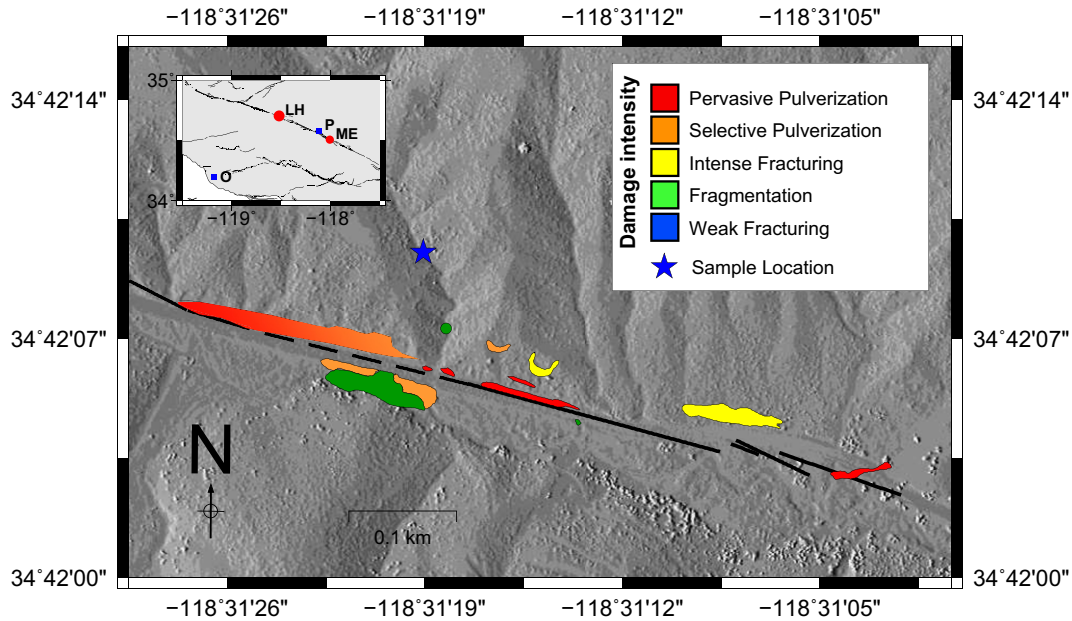
Fig. 3. Location of the samples used in the experiments. We overlay the pulverization map of Dor et al. (2006) and the location of the samples (blue star). We use the same color code as in Dor et al. (2006): red denotes pervasive pulverization, when all crystals in the sample can be crushed by hand; orange for selective pulverization, when some crystals remains intact; yellow for intense fracturing, when crystals retain the original grain size; green for distributed fracturing at the centimeter scale. Our sample can be classified as weakly fractured, with macroscopic large fractures visible in Fig. 5. The digital elevation data were obtained from the GEON project (Prentice et al., 2009). The map was made using Generic Mapping Tools (GMT) software (Wessel and Smith, 1998), using a basic cylindrical projection with a central meridian of longitude equal to −118°30 and a standard parallel of latitude equal to 34°42. The inserted map shows location of some outcrops included in the text: Lake Hughes (LH) outcrop from which the samples for laboratory experiments were taken, Mont Emma Road (ME) outcrop, from which thin sections were made within pulverized rocks (Fig. 1). We also added the location of two major cities of the area, Palmdale (P) and Oxnard (O) (For interpretation of the references to colour in this figure legend, the reader is referred to the web version of this article.).

Three final states could be observed macroscopically:

1. the sample was not damaged
2. the sample was split axially in a few fragments, no more than 5. This is the typical damage observed when a rock sample is uniaxially loaded at low strain rate (Paterson and Wong, 2005).
3. the sample was shattered in multiple small fragments, smaller than the initial grain size of about 1.5 mm. This diffuse damage is reminiscent of pulverized rocks.

No intermediate state was observed between single fracturing and pulverization. Above a strain rate of 150/s, samples are pulverized
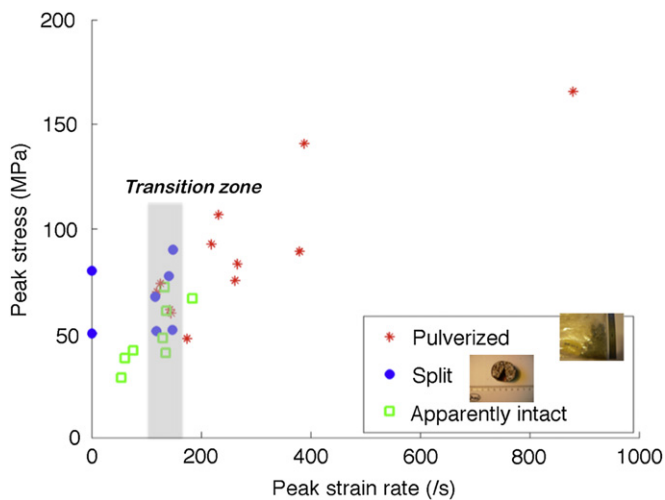
Fig. 4. Final states of damage after dynamic loading of granite from the San Andreas Fault. Results are gathered in a diagram showing strength versus maximum peak strain. There is a transition from single fracturing to multiple fragmentation at strain rates above 150/s (Doan and Gary, 2009).

and there is a sudden transition from failure along a small number of fractures to a pervasively pulverized damage. Doan and Gary (2009) infer that pulverized rocks in the field are the product of coseismic damage, with a strain rate larger than 150/s. They show that such a strain rate is not expected for usual earthquakes propagating at subshear rupture speed. They explain the origin of pulverized rocks as the damage generated by a shock wave, like the Mach wave accompanying a supershear rupture. A Mach wave is a solitary wave that decays slowly with distance. Bhat et al. (2007) show evidence of coseismic damage generated during a supershear rupture up to 5 km from the fault trace. A prediction of our experimental results is that the samples could be pre-damaged before testing, even though they were sampled 150 m from the fault core, a distance at which fracture density levels to the background level for most faults (Mitchell and Faulkner, 2009; Savage and Brodsky, 2011).

Several observations indeed suggest that, though not pulverized, the natural rock used in the first series of experiments was severely damaged. Fig. 5a shows a thin section of the initial state of one of the samples before loading. At the centimetric scale, microfractures are visible from inspection of the whole thin section. At higher magnification, microfractures are also visible at the millimetric and submillimetric scale. The sample is cohesive enough to withstand coring and moderate loading. Yet, experiments described in the next section give an uniaxial strength below 100 MPa, a low value for granitic rock (usually close to 200 MPa, as for Westerly granite (Heap and Faulkner, 2008)).

To investigate the effect of this initial damage on the high strain rate behavior of crystalline rocks, we conducted a further series of experiments of intact granitic rocks.

2.3. Experiments performed on intact rocks

To investigate the effect of damage, we used granite samples from Tarn, France. Fig. 6 shows a thin section of this rock and of the
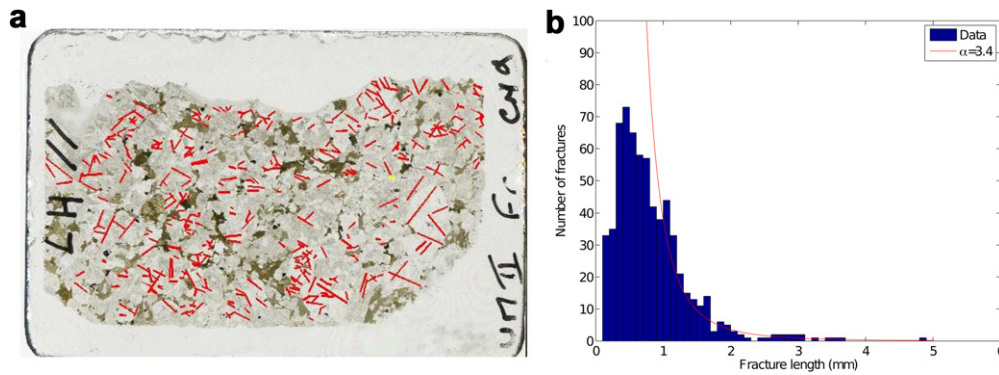
Fig. 5. (a) Thin section cut from a sample from the San Andreas Fault zone, before experiments. The thin section is 4.5 cm long and 2 cm wide. A total of 660 fractures are delineated. (b) Histogram of fracture lengths m delineated in figure (a). Most fractures are smaller than 2 mm. This length corresponds to a. The red line gives a power law fit, $p(l) \propto l^{-\alpha}$, of the fracture length distribution, with a power exponent $\alpha = 3.4$. The fit is poor for small lengths since statistics are not complete for small lengths.

San Andreas Fault rock for comparison. In both cases, the sample is granitic in composition, with a millimetric grain size, significantly smaller than the sample dimension (2.5 cm in diameter, about 2 cm in length). As with the granite near the San Andreas Fault, Tarn granite is slightly weathered, with mechanical alteration of the feldspar grains. Table 1 shows a similar modal composition for both rocks. Hence, we use the Tarn granite as a proxy for the intact, undamaged San Andreas Fault rocks.

Experiments on the Tarn granite are summarized in Fig. 7. It shows three distinct final macroscopic states (Fig. 8): intact, split in to a few fragments, or finely fragmented, equivalent to experiments on the SAF granite (Fig. 4). There is no intermediate state between the two latter stages, at least for the strain rates explored here.

Due to the loading duration being controlled by the striker length, there is always an ambiguity between strain rate and total strain accumulated (Doan and Billi, 2011). To compensate for this artifact, we used different strikers. We also used a pulse shaper to smooth the loading front (Chen and Song, 2010).

As shown in Figs. 7 and 9, pulverization can occur at both low and large strains. Very large strains are attained when the sample is pulverized and multiple fragments are ejected: the sample is no longer present to separate the input and output bars and we record artificially large strains.

There are fewer tests completed on the intact Tarn granite than on the pre-damaged San Andreas samples, yet a transition is still visible if we plot strength versus peak strain rate (Fig. 8). When loading at strain rates above 250/s, samples of Tarn granite fragment into fine grains. The transition threshold is larger than for the pre-damaged case. Rock strength also increases from 75 MPa to 150 MPa when the initial sample is less damaged.

One may speculate on the validity of the comparison between the experiments, as the high strain rate experiments were not conducted on the exact protolith of the damaged Lake Hughes granite. However, our results are consistent with two other studies, suggesting that our experiments are valid. The first is a series of experiments made on Westerly Granite by Yuan et al. (2011). This

paper has an outline very similar to Doan and Gary (2009), but is an independent study. They tested with Split Hopkinson Pressure Bars intact samples of Westerly Granite in unconfined and quasi-oedometric confined conditions. They find in unconfined conditions a transition to pulverization for strain rates above 250/s. The strength threshold was also about 150 MPa. The second is a theoretical model of pulverization developed by François Hild and co-authors (Hild et al., 2003b; Denoual and Hild, 2000), that is in agreement with our experimental results. This theory is presented in more detail within the next section, as we will use it to extrapolate our experimental results in the case of multiple loadings.

3. Statistical theory of pulverization

We studied experimentally the two extreme cases of (1) a pre-damaged sample and of (2) an intact sample. To generalize the conclusions drawn from our experimental data to any level of initial damage, we will refer to the theoretical model of transition from single fracturing to multiple fragmentation, that has been proposed by Hild, Denoual and co-workers (Denoual and Hild, 2000, 2002; Hild et al., 2003a, 2003b). This is a statistical theory that determines the strength of a brittle material, depending on whether it is fractured or pulverized. It is a variant of the Weibull statistical theory of strength. After reviewing the Weibull theory for the common low-strain-rate case, we will present the theory of the high strain rate case proposed by Denoual and Hild (2000). Once the two theories are described, a transition between them can be predicted. This section is mathematically-intensive. Symbols used in equations are summarized in Tables 2 and 3.

3.1. Description of the theory

3.1.1. Weibull hypotheses of rock failure

The Weibull model (Weibull, 1951) is a popular model to describe the failure of a sample by a single fracture. In a sample, there exist initial flaws, with different lengths, and hence different

Table 1
Modal composition of the rocks tested. Modal analysis was performed by random selection of 105 points of the available thin sections (two for the San Andreas Fault samples, one for the Tarn Granite). 95% confidence interval of the proportion of each mineral (in percent) is given between square brackets below the average composition.

Sample	Quartz	K-Feldspar	Plagioclase	Biotite	Amphibole, sphene
San Andreas Fault	28.7%	33.3%	20.3%	16.0%	1.6%
Thin section 1	[24.5–33.3]	[28.8–38.1]	[16.5–24.5]	[12.6–19.9]	[0.6–3.5]
San Andreas Fault	28.2%	35.1%	19.9%	14.9%	1.9%
Thin section 2	[24.0–32.8]	[30.7–40.0]	[16.3–24.1]	[11.7–18.7]	[0.8–3.8]
Tarn Granite	32.8%	39.4%	13.8%	14.1%	0%
	[28.4–37.4]	[34.8–44.1]	[10.6–17.4]	[10.9–17.7]	[0–0.9]
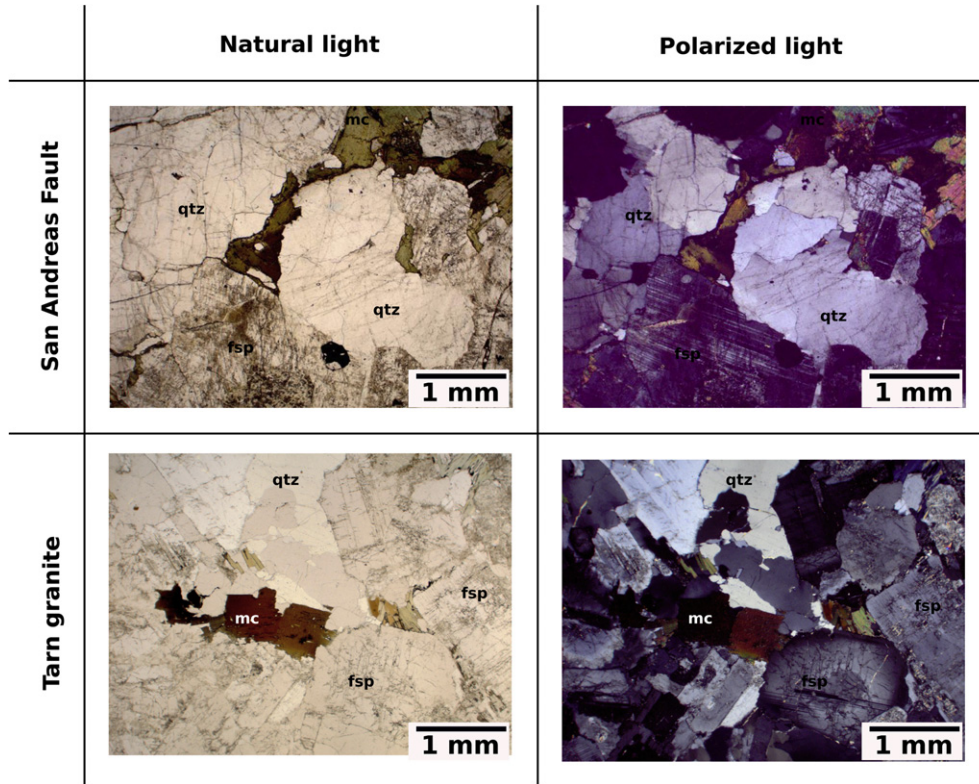
Fig. 6. Thin sections representative of the lithologies tested during the experiments described in this paper. Several minerals are visible: quartz (qtz), feldspar (fsp), mica (mc). Grain size is millimetric in both cases, and therefore much smaller than the sample size. Modal analysis made on the whole thin sections is given in Table 1.

strengths (Fig. 10a). The Weibull model assumes (1) that all flaws are loaded by the same stress, (2) that each flaw will have an independent probability to fail and (3) the breaking of a single fracture will induce the failure of the whole sample; this is the *weakest link hypothesis* (Fig. 10b).

Conditions (1) and (2) assume that the fracture density is low enough for fractures to develop independently, without stress-shadowing effects. If the load is heterogeneous, Hild et al. (2003b) introduced the concept of an effective volume $V_{eff} = Z_{eff}V$ to describe the homogeneously loaded portion of a sample in a rock.

Condition (3) can be understood with concepts from linear elastic fracture mechanics. Fractures act as stress concentrators. Linear elastic fracture mechanics states that at the tip of a fracture of length l, the stress σ is amplified as:

$$\sigma_{ij} = \frac{K}{\sqrt{2\pi r}} f_{ij}(\theta) \tag{1}$$

r is the distance to the fracture tip and θ the orientation to the fracture angle. f_{ij} is a known adimensional function. K is the stress intensity factor. Depending on the loading mode, the detail of its expression varies, but it retains the general form:

$$K = Y\sigma\sqrt{l}, \tag{2}$$

where Y is an adimensional geometrical factor and σ is the amplitude of the loading. For instance, for a mode I loading $K = \sigma\sqrt{\pi l}$.

Irwin (1957) have shown that if K exceeds a threshold value K_c then the fracture extends to reach a longer length l. According to Eq. (2), the stress intensity factor then increases. K_c could then be reached with a smaller stress σ: the strength of the fracture is smaller. This positive loopback explains why the failure of a major

flaw can develop catastrophically into the complete failure of the sample (Fig. 10b).

From a uniform stress field σ and a given fracture mode, Eq. (2) predicts that a fracture will fail if it exceeds a threshold length

$$L_c = \left(\frac{K_c}{Y\sigma}\right)^2 \tag{3}$$

We now explore the probability for the occurrence of a fracture longer than L_c.

3.1.2. Weibull statistical model of single fracturation

In most natural samples there is an initial network of fractures. The initial fracture density is labeled λ_0. If we take a volume V, there is on average a number of N fractures within this volume, with $N = \lambda_0 V$. Fracture density is not the only fracture parameter controlling the sample strength. The length distribution of these fractures is also important. Each fracture has a probability of having a length between l and $l + dl$ given by the probability distribution function $p(l)$. The average density of fractures λ_{L_c} of length greater than a critical length is then $\lambda_{L_c} = \lambda_0 \int_{L_c}^{\infty} p(l)dl$. Hence, the probability of having k fractures of length greater than L_c within the volume V is then given by the Poisson statistics:

$$p_{V,L_c}(k) = \frac{(\lambda_{L_c}V)^k}{k!} e^{-\lambda_{L_c}V} \tag{4}$$

In the weakest link hypothesis, the probability of survival of the sample is given by $p_{V,L_c}(k = 0)$. If the sample does not survive, it fails, and hence the probability of failure is given by

$$p_F = 1 - p_{V,L_c}(0) = 1 - e^{-\lambda_{L_c}V} \tag{5}$$

Sample	Peak strain rate (/s)	Peak stress (MPa)	Peak strain (%)	Final state	Photograph
T1	708	313	4.12	Pulverized	No picture
T2	51	97	0.25	Intact	No picture
T7	755	201	8.26	Pulverized	
T9	518	159	4.74	Pulverized	
T10	150	126	0.13	Split	
T12	180	162	0.32	Split	
T13	289	160	0.66	Pulverized	
T14	258	144	0.74	Split	
T15	217	139	0.51	Split	
T17	251	153	0.56	Pulverized	

Fig. 7. Summary of experiments performed on Tarn granite. For each sample, peak stress, peak strain, peak strain rate and a classification of the final damage are reported. When available, a photograph illustrating the post-mortem macrodamage of the sample is also included. The ruler in the photographs is graduated in centimeters.

This relationship scales with the volume under consideration (Weibull, 1951). For instance, if we are interested in a volume $\mathbb{V} = v \times V$, there is no failure in the volume $\mathbb{V}$ if there is no failure within all the v volumes of size $\mathbb{V}$. All these events are independent and we obtain

$$p_{\mathbb{V},L_c}(0) = \left(p_{V,L_c}(0)\right)^v = e^{-\lambda_{L_c} v V} = e^{-\lambda_{L_c} \mathbb{V}} \tag{6}$$

Eq. (5) holds if we replace V by a larger volume $\square$. The expression of Weibull law is scale independent. Let us assume now that the size distribution $p(l)$ can be described by a power law $p(l) = Cl^{-\alpha}$, where C is a normalizing factor, dependent on the smallest fracture length. Then, we obtain a simple expression for λ_{L_c}:

$$\lambda_{L_c} = \lambda_0 \int_{L_c}^{\infty} Cl^{-\alpha}dl = -\lambda_0 C\frac{L_c^{1-\alpha}}{1-\alpha} \tag{7}$$

Using the above equation and Eq. (2), Eq. (5) then reduces to a Weibull distribution:

$$p_F = 1 - e^{-\left(\frac{\sigma}{\Delta\sigma}\right)^m} \tag{8}$$

where $m = 2(\alpha-1)$ and $\Delta\sigma = (K_c/Y)(m/2CV\lambda_0)^{1/m}$. m is called the shape parameter and $\Delta\sigma$ the scale parameter of the Weibull distribution. The maximum of the associated probability density function is reached at for $\sigma_{\max} = (m-(1/m))^{1/m}\Delta\sigma$ if $m > 1$. From Weibull equations, we obtain the average strength of a sample (Fig. 11):

$$\sigma_{F,\text{static}} = \int_0^{\infty} \frac{dp_F}{d\sigma}\sigma d\sigma = \frac{\Delta\sigma}{m}\Gamma\left[\frac{1}{m}\right] \tag{9}$$

where $\Gamma[x] = \int_0^{\infty} t^{x-1}e^{-t}dt$ is the gamma special function. Therefore the strength of the sample decreases with the initial density of
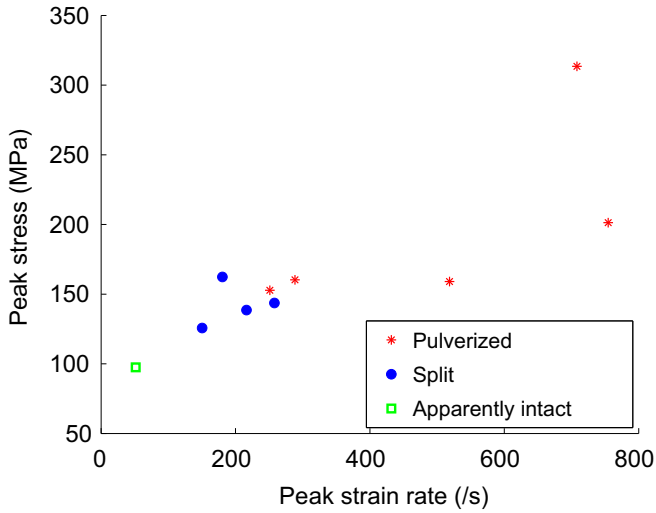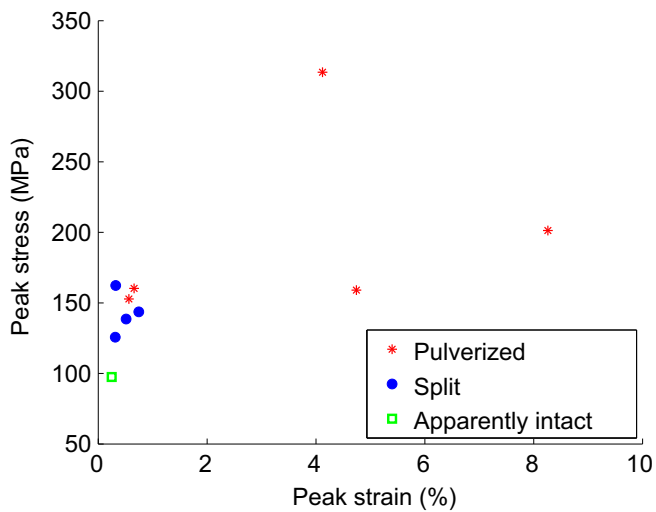
Fig. 8. Final states of damage after dynamic loading of Tarn granite. Results are gathered in a diagram showing strength versus maximum peak strain. As in Fig. 4, there is a transition from single fracturing to multiple fragmentation, but at a higher strain rate, above 250/s.

Table 2
Table of symbols used within the equations of the text – Latin alphabet.

Symbols	Meaning
c	Stress wave velocity
e	Euler number (~ 2.718)
K	Stress intensity factor
l	Length of fracture
L_c	Threshold length of fracture, for which $K > K_c$ or L_c. Fractures longer than L_c will propagate
m	Shape parameter of Weibull distribution. Representative of the sample homogeneity.
n	Number of dimensions of the problem (here 3)
p_F	Probability of failure
P_{ns}	Probability for a fracture longer than L_c to be not overshadowed by another fracture
$p_{V,L_c}(k)$	Probability of having k fractures of length greater than L_c within the volume V
t_c	Characteristic time for a fracture to be interacting with surrounding fracture
t_f	Characteristic time for a fracture to reach failure under a constant stress rate $\dot{\sigma}$
V	Volume of the sample
V_{eff}	Volume uniformly loaded by stress σ
Y	Geometrical factor intervening in stress intensity factor computation
Z_{eff}	Ratio between V_{eff} and V

fractures λ_0 and with its volume, as we have more chance to find a fracture of critical length.

The Weibull model also recognizes that the heterogeneity of samples leads to a variability in sample strength. The standard deviation in sample strength is given as $\Delta\sigma_{F,static} = \Delta\sigma\sqrt{\Gamma(1 + (2/m)) - (\Gamma(1 + (1/m)))^2} \sim (\pi\Delta\sigma/\sqrt{6}m)$. This means that if m is very large, the Weibull distribution is very peaked, and hence has a more uniform strength distribution. By playing between the shape parameter m and the scale parameter $\Delta\sigma$, we can quantify the heterogeneity and the weakness of the sample. The Weibull model statistically predicts the strength of a sample based on microscopic fracture lengths (Jayatilaka and Trustrum, 1977).

To check the validity of the Weibull model for single-fracture samples, we estimated the m Weibull parameter for the pre-damaged San Andreas Fault samples using two approaches (Fig. 12). Fig. 5b gives the length distribution of fractures picked from a thin section, at a centimetric scale. The limited resolution of the image prevents the completeness of the fracture catalog for smaller fractures. Yet, the length distribution of the largest fractures can be roughly matched (Fig. 5) with a fractal coefficient $\alpha = 3.4$, giving an exponential value of $m = 2(\alpha - 1) = 4.8$. This result is slightly larger than the particle grain size distribution found with a laser granulometer by Wechsler et al. (2011), who obtained a grain size distribution matching a power law function with a coefficient α ranging from 2.5 to 3.1 for pulverized rocks collected in a borehole near Mount Emma outcrop along the San Andreas Fault (Fig. 3). We then determined the strength distribution for the samples that were split. The cumulative strength distribution is fitted with a Weibull distribution. We find a scale parameter $\Delta\sigma = 70$ MPa and a shape parameter $m = 5$, that is similar to the experimental value $m = 4.8$ found by fitting the microfracture length distribution. The Weibull theory gives satisfactory results for the samples that were pre-fractured.

Fig. 9. Strain dependence on the transition from single fracturing to multiple fragmentation, from the summary of experiments in Fig. 5. The extremely damaged, pulverized rocks can withstand loading to artificially large strains; however, two cases (T13 and T17) also show that pulverization can occur at smaller strain.

Table 3
Table of symbols used within the equations of the text – Greek alphabet.

Symbols	Meaning
α	Coefficient of the power law governing fracture length statistics
$\gamma(\nu,x)$	Lower incomplete Gamma special function
$\Gamma(x)$	Gamma special function
$\Delta\sigma$	Scale parameter of Weibull distribution. Representative of the sample strength.
$\Delta\sigma_{F,static}$	Standard deviation of the strength statistics of a sample quasi-statically loaded
λ_0	Initial fracture density
λ_b	Density of fractures amenable to further propagation and that effectively break
$\lambda_{b,sat}$	Maximum density of fractures that effectively break, at saturation
λ_s	Density of fractures amenable to further propagation but stress-shadowed by other fractures
λ_{L_c}	Density of fractures of length longer than L_c, i.e. of fracture amenable to propagation
σ	Applied stress
$\dot{\sigma}$	Stress rate
$\dot{\sigma}_c$	Transition stress rate from single fracture to multiple fragmentation
$\sigma_{F,dyn}$	Average strength of a sample loaded at high strain rate
$\sigma_{F,static}$	Average strength of a sample quasi-statically loaded
Ω_0	Initial size of the shadow zone around a fracture
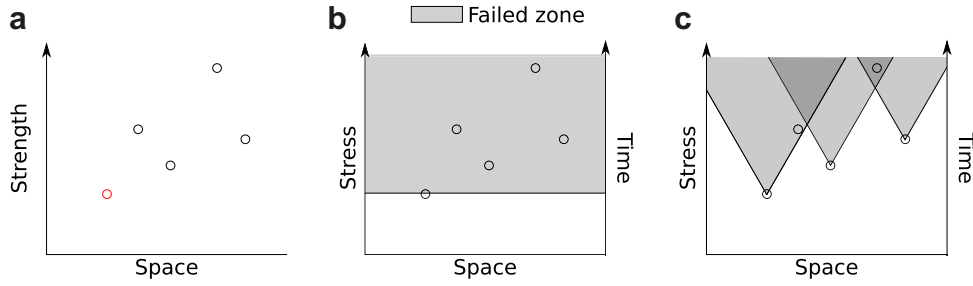
Fig. 10. Schematics of the different theories of failure. (a) Initial flaw model: There is an initial distribution of flaws scattered in space, with different locations, and different strengths. The sample is then loaded at a given stress rate (or strain rate in an elastic solid). There are two extreme cases: (b) Slow strain rate case: The sample is loaded so slowly that the propagation of the weakest flaw is considered instantaneous. Breaking the weakest flaw leads to the failure of the whole sample. (c) High strain rate case: The sample is loaded so rapidly that the finite fracture propagation speed cannot be ignored. This allows the propagation of multiple fractures at the same time. Yet not all fractures propagate, as some can be stress shadowed by other propagating flaws.

3.1.3. The Hild model of multiple fragmentation

When a sample is loaded rapidly, the physics of the interaction between flaws is altered (Fig. 10c). Stress wave propagation has to be taken into account. The weakest flaw takes a finite time to expand, during which time other cracks can also expand. But during that time, some fractures can also enter the shadow zone of others. Hence, the Weibull model has to be modified to take into account these two phenomena. This is what is achieved with the theory of Hild et al. (2003b), which we will summarize and reformulate in this section. Let us assume that a stress σ is applied homogeneously on the material. We saw in Section 3.1.2 that there

is an average density of fractures λ_{L_c} that may break for a stress smaller than σ. Combining Eqs. (3) and (7), λ_{L_c} expresses as

$$\lambda_{L_c} = \lambda_0 \frac{2C}{m} \left(\frac{Y\sigma}{K_c} \right)^m \tag{10}$$

However, only a fraction λ_b of them effectively break, as some are stress-shadowed. The density of shadowed fractures is denoted by λ_s.

$$\lambda_b = \lambda_{L_c} - \lambda_s \tag{11}$$

Let us assume that the area shadowed by an expanding flaw expands as $\Omega(t) = \Omega_0 \times (c(t-t_0))^n$, where n is the dimension of the problem (here $n = 3$), c is the fracture propagation speed, Ω_0 an adimensional coefficient controlling the size of the shadow zone and t_0 the start of fracture propagation. The sample is progressively loaded and stress increases with time: $\sigma = \dot{\sigma}t$. In the case of a purely brittle material, this is equivalent to loading at a constant strain rate. Let us suppose we are now at time t. At $t + dt$, we reach the stress $\sigma + (d\sigma/dt)dt$. At this higher stress, new cracks will begin to break, provided that their strength is between σ and $\sigma + (d\sigma/dt)dt$ and that they are not overshadowed:

$$\frac{d\lambda_b}{dt} = \frac{d\lambda_{L_c}}{dt} P_{ns} \tag{12}$$

We now address the question of how to compute P_{ns}, the probability not to be shadowed? A flaw is not overshadowed if there is no initial fracture on its horizon during previous time steps (Fig. 13). To estimate this, let us consider the probability that a fracture can be overshadowed by another fracture that would have initiated at time t_0 and $t_0 + dt_0$. This is equivalent to slicing the horizon (dashed lines of Fig. 13) several times between t_0 and t_0+dt_0 (horizontal lines of Fig. 13). This is given by the Poisson process that involves the probability of finding a fracture of strength $(d\lambda_{L_c}/d\sigma)(d\sigma/dt)dt = d\lambda_{L_c}/dt|_{t_0} dt_0$ in the affected volume $\Omega(t-t_0)$. The probability that no fracture appears is

$$dP_{ns} = \exp\left(-\frac{d\lambda_{L_c}}{dt} \bigg|_{t_0} \Omega(t - t_0) dt_0 \right) \tag{13}$$

We then integrate Eq. (13) for all previous time steps, until $t_0 = 0$, using the scaling relationship of the Weibull distribution (Eq. (6)). The probability for a fracture not being shadowed is then:
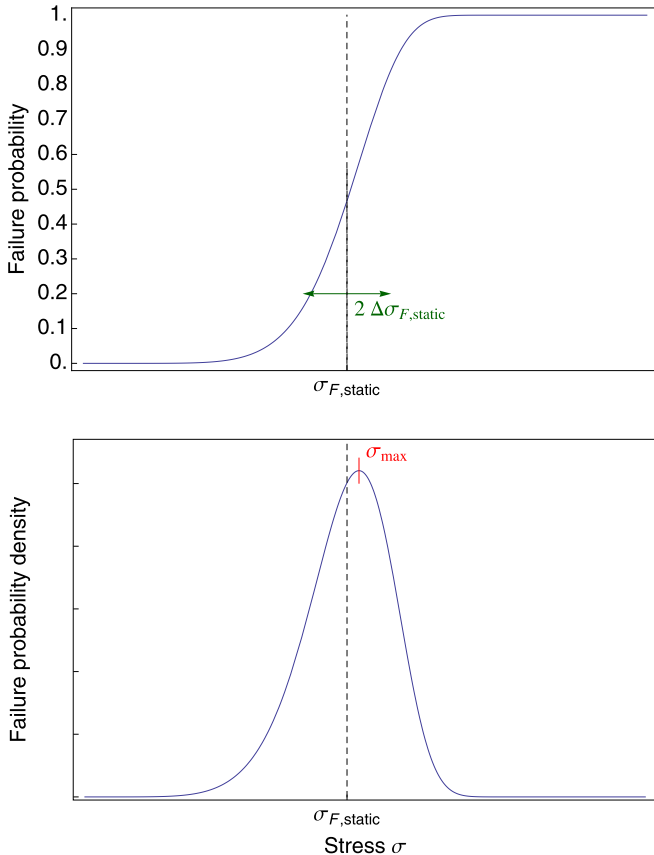
Fig. 11. Failure probability predicted by Weibull equation (Eq. (8)). The shape parameter m and the scale parameter $\Delta\sigma$ control the values of σ_{av} (Eq. (9)) and σ_{max}. In this graph, $m > 1$.

$$P_{ns} = \exp\left(-\int_0^t \frac{d\lambda_{L_c}}{dt} \bigg|_{t_0} \Omega(t - t_0) dt_0 \right) \tag{14}$$
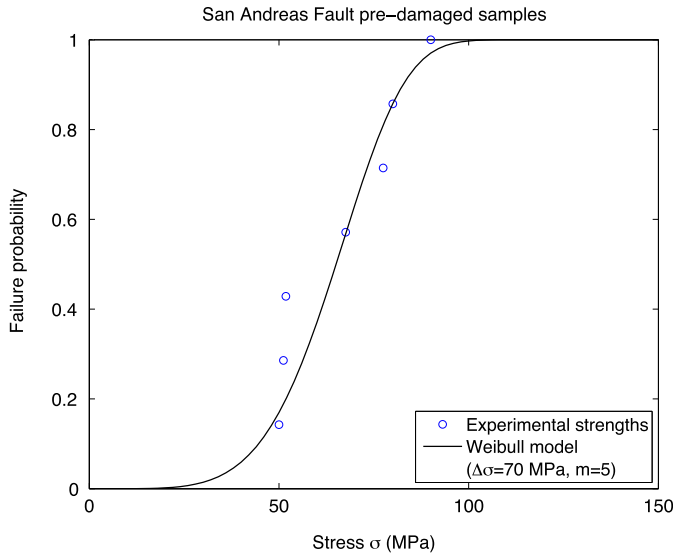
Fig. 12. Experimental determination of the Weibull parameters for the pre-damaged samples from the San Andreas Fault. We consider only the strength of the samples that were single-fractured. The cumulative probability density function is then fitted with a cumulative Weibull distribution, as in Fig. 11. Experimental Weibull parameters are $\Delta\sigma = 70$ MPa and $m = 5$.
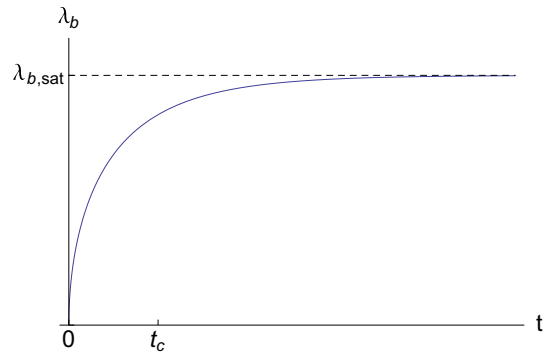
We then integrate this equation using the expression of λ_{L_c} from Eq. (10) to obtain

$$P_{ns} = \exp\left[-\lambda_0 \frac{2C}{m}\Omega_0 c^n \frac{m!n!}{(m+n)!} t^{m+n}\left(\frac{\dot\sigma Y}{K_c}\right)^m\right] \quad (15)$$

Note that we can simplify the above expression as $P_{ns} = e^{-(m!n!/(m+n)!)\lambda_{L_c}(t)\Omega_0(ct)^n}$, but we prefer to write $P_{ns} = e^{-(t/t_c)^{m+n}}$ to highlight the characteristic time for fracture interaction through stress waves:
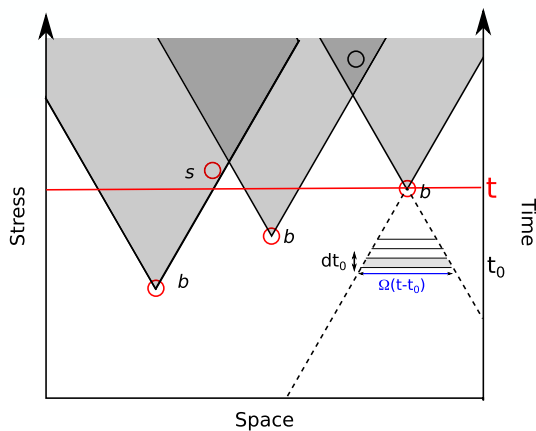
Fig. 13. Graphical representation of the concepts developed in the case of multiple fractures. For a given stress, there are a few preexisting flaws that have a lower stress than σ (red circle, labeled with a subscript c in the main text). Some of them are effectively initiated (subscript b) and their shadow zones (shaded areas) expand as they propagate. Others flaws cannot be activated (subscript s) because they fall within the shadow zone of an initiated crack. To investigate the probability of falling within a shadow zone, we delineate the horizon of the fracture (dashed lines) projected backwards in time, or equivalently backwards in stress as $\sigma = \dot\sigma dt$. The probability that a crack breaks is computed by combining the probability for an existing flaw to be within the influence area between t_0 and $t_0 + dt$ (For interpretation of the references to color in this figure legend, the reader is referred to the web version of this article.).

$$t_c = \left[\frac{2C\lambda_0\Omega_0 m!n!c^n\left(\frac{\dot\sigma Y}{K_c}\right)^m}{m(m+n)!}\right]^{-\frac{1}{m+n}} \quad (16)$$

The equation is rather large, yet it expresses some intuitive ideas: the characteristic time for fracture interaction decreases with the initial density of fractures λ_0, with the loading rate $\dot\sigma$, the minimal size of the shadow zone around each Ω_0 and with the stress wave velocity c. The characteristic time t_c is to be compared with another characteristic time: the time t_f for the loading to lead to new fracture t_f. We can re-express Eq. (10) as $\lambda_{L_c} = \lambda_0(t/t_f)m$ with
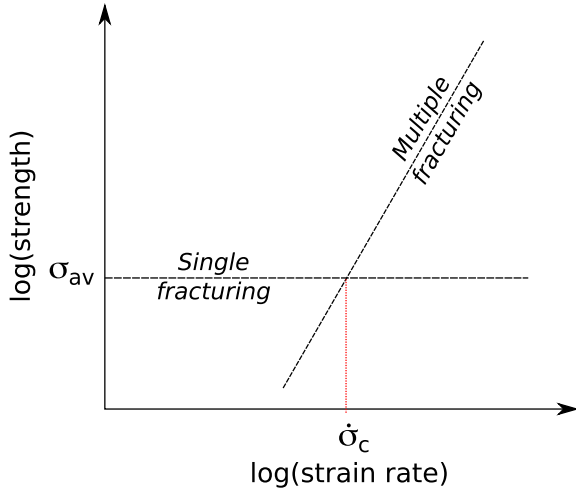
$$t_f = \frac{K_c}{\dot\sigma Y}\left(\frac{m}{2C}\right)^{\frac{1}{m}} \quad (17)$$

From Eqs. (10), (12) and (15), we derive λ_b, the density of fractures that will effectively break at stress σ:

$$\lambda_b = \lambda_0 \frac{m}{m+n}\left(\frac{t_c}{t_f}\right)^m \gamma\left[\frac{m}{m+n},\left(\frac{t}{t_c}\right)^{m+n}\right] \quad (18)$$

where $\gamma[\nu,x] = \int_0^x t^{\nu-1}e^{-t}dt$ is the lower incomplete gamma function. The time evolution predicted by the above equation is given by Fig. 14. As $\gamma[\nu,t] \underset{t\sim 0}{\sim} (t^\nu/\nu)$ at short times, $\lambda_b \sim \lambda_0(t/t_f)^m$: the more homogeneous the distribution of flaw strengths, the higher is m, and the more sudden is the simultaneous growth of fractures. Note that at small times, $\lambda_b(t) \sim \lambda_{L_c}(t)$: the stress-shadowing phenomenon is not yet efficient. The breaking fractures density saturates rapidly to $\lambda_{b,sat} = \lambda_0(m/m+n)\Gamma[m/m+n](t_c/t_f)^m$, where $\Gamma[x]$ is the Euler gamma function ($\Gamma[\nu] = \gamma[\nu,\infty]$). We see that the density of fractures that will effectively break increases if the shadowing process is slow (large t_c) compared to the fracture initiation duration t_f. The above equation can be expressed in terms of applied stress rather than time, by introducing a critical stress $\sigma_c = \dot\sigma t_c$. The critical stress scales as $\dot\sigma^{n/m+n}$.

Computing analytically the strength of the sample is difficult. We can no longer use the Poisson process underlying the Weibull Eq. (5) as the failures of all subparts of the samples are not independent events anymore, because of the stress-shadowing process. Instead, Denoual and Hild (2000) use a mean-field theory by introducing the concept of macroscopic damage D to exploit the density of broken fractures. They take as a proxy of damage the probability $D = 1 - P_{ns}$. This damage parameter is then inserted in a mean-field theory of stress screening, similar to the strategy developed by Grady and Kipp (1989): the stress that has been considered so far is an effective stress that is different from the applied stress $\sigma_{app} = (1-D)\sigma$. The dynamic strength $\sigma_{F,dyn}$ of the

Fig. 14. Time evolution of breaking fracture with time, as predicted by Eq. (18). The fracture population increases with a power law of time, but saturates due to stress-shadowing between propagating fractures.

Fig. 15. Strength depends on the pulverization regime. In the case of a single fracture, strength is independent of strain rate. In case of pulverization, strength is a power law of strain rate. The transition between the two regimes happens for a characteristic stress $\dot{\sigma}_c$.

sample is the maximum of the stress applied during the loading. This happens when $(d\sigma/dt) = (d/dt)((\dot{\sigma}t)P_{ns}) = 0$, *i.e.* for $t_{max} = (1/m + n)^{(1/m+n)}t_c$. The maximum applied stress is therefore $\sigma_{F,dyn} = e^{-1/m+n}\sigma_c$, whose full expression is

$$\sigma_{F,dyn} = \left[\frac{2eC\lambda_0\Omega_0 m!n!c^n\left(\frac{Y}{K_c}\right)^m}{m(m+n)!}\right]^{-\frac{1}{m+n}} \dot{\sigma}^{\frac{n}{m+n}} \tag{19}$$
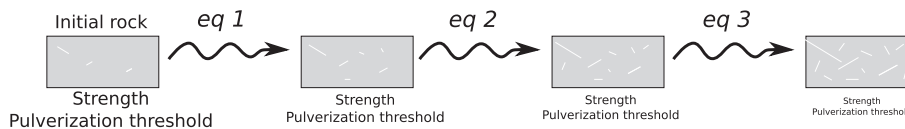
Dynamic strength increases with strain rate, with a power law of exponent $(n/m + n)$. Higher strain rate indeed results in smaller fragments, as shown by the experiments of Section 2 but also by Grady and Kipp (1989). This increases the fracture energy created during damage of the rock. This contrasts with the quasi-static loading case, for which strength is independent of strain rate.

3.2. Prediction on the effect of damage on the transition

These theoretical results show that rock strength varies with stress rate (hence for a pure brittle solid, with strain rate). The variation is schematically described in Fig. 15. For a single fragmentation problem, strength is constant. For a multiple fragmentation problem, strength increases as a power law of stress rate. The transition between the two regimes happens when $\sigma_{F,static} = \sigma_{F,dyn}$. If we use the damage theory of Denoual and Hild (2000), we get a transition strain rate of

$$\dot{\sigma}_c = \left(\frac{2C\lambda_0}{m}\right)^{-\frac{1}{m}} \frac{K_c c}{Y} \left[\frac{e\Omega_0 n!m!}{(m+n)!}\right]^{\frac{1}{n}} \left(\frac{\Gamma\left[\frac{1}{m}\right]}{m}\right)^{\frac{m+n}{n}} V^{-\frac{m+n}{mn}} \tag{20}$$

This can be also more compactly written as

$$\dot{\sigma}_c = \left[\frac{e\Omega_0 n!m!}{(m+n)!}\right]^{\frac{1}{n}} \left(\frac{\Gamma\left[\frac{1}{m}\right]}{m}\right)^{\frac{m+n}{n}} \Delta\sigma c V^{-\frac{1}{n}} \tag{21}$$

The threshold in stress rate depends on $\Delta\sigma$, the scale parameter of the Weibull distribution used in the static case, divided by the characteristic time for elastic wave to travel the sample $V^{(-1/n)}/c$ and by an adimensional factor that depends on the shape parameter m of the Weibull distribution, *i.e.* the initial fracture size distribution of the sample. This highlights several features. The transition threshold $\dot{\sigma}_c$ from single fracturing to fragmentation decreases with the initial density of fractures λ_0, with an exponent $1/m$. It also decreases with the volume V of the rock loaded, with an exponent $(m + n/mn)$. The homogeneity of the sample, described by the Weibull shape parameter m, also affects the transition threshold. The three parameters also affect the static strength of the sample (Eq. (9)).

The size dependence might have been problematic to the applicability of our experiments to a fault zone. Yet, pulverized rocks are recognized in the field as (1) a rock sample that is easily crushed within a person's hand and (2) as a rock whose initial structure is preserved, *i.e.* a rock that has experienced little strain. Condition (1) is tested with samples a few centimeters long, which is the size of our experimental samples. Hence, we consider that the strength and transition from single fracturing to fragmentation determined from our experiments are valid.

The theory predicts a diminution of the strength and the transition threshold to pulverization with initial damage, as they both scale as $\lambda_0^{(-1/m)}$. This confirms the experimental results of Section 2. The intact rock has a static strength of about 150 MPa and a transition strain rate of about 250 s^{-1}. The pre-damaged rock has a strength of 75 MPa, only half the strength of the intact rock. The transition strength for the pre-damaged rock also decreases by almost a factor of two, falling to about 150 s^{-1}. Hence, the theory provides a correct prediction of our experimental results.

4. Application to active faults: development of a zone of pulverized rocks after multiple earthquakes

The diminution of the strength and of the pulverization threshold suggests a scenario for pulverization along active faults in which rocks are pulverized by successive earthquakes (Fig. 16). A first earthquake loads at high frequency the surrounding rocks. If a rupture generates enough high frequencies, the damage is diffuse: multiple fractures propagate, and any decimetric fragment near the fault zone becomes diffusively damaged. The damage induces a reduction in strength of the rock near the fault. It also lowers the threshold in strain rate to switch from localized damage to diffuse damage (*i.e.* pulverization). It would be easier for the next earthquake to also damage diffusively all the rocks around the fault zone. With successive loadings, the rocks around the fault zone get progressively finely pulverized.

Pulverized rocks have only been identified recently (Wilson et al., 2005). Why don't we see more pulverized rocks? If loading happens at too low a strain rate, damage is localized along a few

Fig. 16. Schematic evolution of damage as successive earthquakes (*eq*) further damage the rock. Both rock strength and the strain rate pulverization threshold decrease with successive earthquakes. This leads to a feedback process whereby diffuse damage is increasingly facilitated during subsequent loadings. In other words, the rock becomes progressively pulverized.

fractures. In the portions which experienced little fracturing, their strength and strain rate threshold to pulverization are not modified. Hence, further loading would localize on the weak fractured area but not on the background rock left intact. The diffuse damage pattern found in outcrops of pulverized rocks would not be found if no sufficiently high strain rate loading occurred. Doan and Gary (2009) have demonstrated that such high strain rate loading is rare but may occur, for instance, associated with supershear earthquakes.

The feedback process described above may explain the commonly observed decrease in damage with distance from the fault, including in the case of pulverized rocks. Faulkner et al. (2010) review published profiles of decay of microfracturing with distance from the fault core. If we compare Fig. 4 of Faulkner et al. (2010) with the microfracture decay profile for the pulverized granite of the Arima-Takatsuki fault (Mitchell et al., 2011), we observe that the decay rate for the pulverized fault is among the highest, and as rapid as for the outcrop described by Vermilye and Scholz (1998). Pulverization is very intense close to the Arima-Takatsuki fault, but decays rapidly with distance, although the absolute microfracture density is above what is typically observed along non-pulverized faults. This is also shown on the pulverization map of the Lake Hughes outcrop (Dor et al., 2006), reported in Fig. 3, where pulverized outcrop is localized in patches. This may be explained by our results. Before pulverization, rocks closer to the fault core are more damaged and hence easier to pulverize. During the first pulverizing events, they get even more damaged than rocks located farther from the fault. With successive events, they would experience intense comminution compared to rocks further away. Pulverized rocks would then be found highly localized close to the fault.

The distribution of pre-damaged rocks may also explain the paradox of the Lake Hughes outcrop along the Mojave segment of the San Andreas Fault (Dor et al., 2006), where pulverized granite and undamaged limestone are found on the same side of the fault. The two rocks are likely to have different strengths and are therefore likely to pulverize in different ways. If earthquakes started to homogeneously damage the granite but not the limestone, the feedback loop described above would further differentiate the two rock behaviors relative to loading. Granite would become progressively damaged and easier to pulverize, while the carbonate rock would stay relatively intact and harder to damage.

Several pulverized outcrops have an asymmetric damage pattern (Dor et al., 2006; Mitchell et al., 2011) that has been attributed to the high frequency tensile pulse on the strongest side generated by an earthquake along a bimaterial fault (Shi and Ben-Zion, 2006). As the strongest side gets more damaged and becomes less strong, mature bimaterial faults may not be able to generate such high frequency pulses. Several arguments are in favor of the persistence of the high frequency pulse: (1) The development of an asymmetric pulse is controlled by mechanical properties at the kilometric scale (2) Pulverized rocks have so far been found only at the surface or at shallow depths (Wechsler et al., 2011). We add a third argument: weaker rocks are more easily pulverized, and if the strongest side experienced pulverization previously, it would become more amenable to further pulverization. This could explain the sharp asymmetry in distribution of pulverized rocks along bimaterial faults.

In this feedback process leading to pulverization, we have ignored the healing process that follows earthquake events. Healing would seal fractures by a wide range of processes that depend on the size of the fractures (Gratier and Gueydan, 2007): thin fractures experience self-healing within days, a process driven by minimization of surface energy, whereas larger fractures require years to heal by pressure solution. Hence large scale-healing of

faults is expected to be driven by pressure solution (Gratier, 2011). Pressure-solution efficiency depends on the solubility of the mineral involved. Dissolution of feldspar and quartz are more efficient at high temperatures, below 5 km depth, whereas dissolution of calcite is more efficient at low temperatures, above 3 km depth for a classical geothermal gradient of 30 K/km (Gratier et al., 2003). For instance, samples taken within the San Andreas Fault at the SAFOD borehole show evidence of intense sealing by calcite, some evidence of feldspar dissolution, but quartz is intact (Gratier et al., 2011). In the case of the pulverized rocks found along the San Andreas Fault, self-healing of former thin fractures is evidenced by the presence of lineaments of inclusion planes. But Fig. 1 shows no sign of dissolution of Feldspar or quartz, consistent with the fact that these rocks were pulverized in the near surface citepWechsler11. As these rocks are crystalline, no calcite cementation is found. Hence pressure solution did not happen within these rocks: only the thin intragranular fractures with no mismatch would heal. This may explain why the pulverized rocks found along the Mojave segment of the San Andreas Fault (Dor et al., 2006) are still damaged whereas the last large recorded event in the area occurred about 150 years earlier (1857 Fort Tejon earthquake).

5. Conclusions

In this paper we have presented several pieces of evidence suggesting that rocks are easier to pulverize when they are pre-damaged. We first presented experimental results from high strain-rate loading experiments on both pre-damaged and intact granite. Pre-damaged granite is pulverized if the strain rate is higher than 150/s. Instead, two independent studies find a strain rate threshold of 250/s for intact granite. The strain rate threshold is roughly proportional to the sample strength at low strain rate. These experimental results are consistent with the statistical theory of high strain rate proposed by Denoual and Hild (2000) and Hild et al. (2003b).

We propose a scenario in which pulverized rocks may result from successive earthquakes, instead of pulverization occurring by a single event. Yet, to initiate the feedback process leading to pulverization, diffuse damage of rocks around the fault is required to occur by high strain rate loading. This suggests that pulverized rocks are markers of extreme loading. This is consistent with the persistent features associated with the process that may generate high frequency waves around a fault: bimaterial faults (Andrews and Ben-Zion, 1995), or the low roughness of segments prone to supershear rupture (Bouchon et al., 2010).

References

Andrews, D.J., Ben-Zion, Y., 1997. Wrinkle-like slip pulse on a fault between different materials. J. Geophys. Res. 102, 553–571.

Bhat, H.S., Dmowska, R., King, G.C.P., Klinger, Y., Rice, J.R., 2007. Off-fault damage patterns due to supershear ruptures with application to the 2001 M_w 8.1

Kokoxili (Kunlun) Tibet earthquake. J. Geophys. Res. 112, 1–19. doi:10.1029/2006JB004425.

Bouchon, M., Karabulut, H., Bouin, M.-P., Schmittbuhl, J., Vallée, M., Archuleta, R., Das, S., Renard, F., Marsan, D., 2010. Faulting characteristics of supershear earthquakes. Tectonophysics 493 (3–4), 244–253.

Chen, W.W., Song, B., 2010. Split Hopkinson (Kolsky) Bar Design, Testing and Applications. Mechanical Engineering Series. Springer, New York.

Denoual, C., Hild, F., 2000. A damage model for the dynamic fragmentation of brittle solids. Comp. Meth. Appl. Mech. Eng. 183 (3–4), 247–258.

Denoual, C., Hild, F., 2002. Dynamic fragmentation of brittle solids: a multi-scale model. Eur. J. Mech. A. 21 (1), 105–120.

Doan, M.-L., Gary, G., 2009. Rock pulverisation at high strain rate near the San Andreas Fault. Nat. Geosci. 2, 709–712.

Doan, M., Billi, A., 2011. High strain rate damage of Carrara marble. Geophys. Res. Lett. 38 (38), L19302. doi:10.1029/2011GL049169.

Dor, O., Ben-Zion, Y., Rockwell, T.K., Brune, J., May 2006. Pulverized rocks in the Mojave section of the San Andreas fault zone. Earth Planet. Sci. Lett. 245, 642–654.

Dor, O., Yildirim, C., Rockwell, T.K., Ben-Zion, Y., Emre, O., Sisk, M., Duman, T.Y., 2008. Geological and geomorphologic asymmetry across the rupture zones of the 1943 and 1944 earthquakes on the North Anatolian Fault: possible signals for preferred earthquake propagation direction. Geophys. J. Int. 173 (2), 483–504.

Dor, O., Chester, J.S., Ben-Zion, Y., Brune, J.N., Rockwell, T.K., 2009. Damage characterization in sandstones along the Mojave section of the San Andreas fault with a new method: implications for the depth and mechanism of rock pulverization. Pure Appl. Geophys. 166 (10–11), 1747–1773.

Faulkner, D.R., Jackson, C.A.L., Lunn, R.J., Schlische, R.W., Shipton, Z.K., Wibberley, C.A.J., Withjack, M.O., 2010. A review of recent developments concerning the structure, mechanics and fluid flow properties of fault zones. J. Struct. Geol. 32 (11), 1557–1575. doi:10.1016/j.jsg.2010.06.009.

Gama, B.A., Lopatnikov, S.L., Gillespie Jr., J.W., 2004. Hopkinson bar experimental technique: a critical review. Appl. Mech. Rev. 57 (4), 223–250.

Grady, D., Kipp, M., 1989. Dynamic rock fragmentation. In: Atkinson, B. (Ed.), Fracture Mechanics of Rocks. Academic Press, pp. 429–475.

Graf, K.F., 1991. Wave Motion in Elastic Solids. Dover Publications.

Gratier, J.-P., Favreau, P., Renard, F., 2003. Modeling fluid transfer along California faults when integrating pressure solution crack sealing and compaction processes. J. Geophys. Res. 108 (B2). doi:10.1029/2001JB000380

Gratier, J.-P., Gueydan, F., 2007. Deformation in the presence of fluids and mineral reactions – Effect of fracturing and fluidâ rock interaction on seismic cycles. In: Handy, M., Hirth, G., Hovius, N. (Eds.), Tectonic Faults. The MIT Press, Cambridge, Massachusetts, USA, pp. 319–356.

Gratier, J.-P., Richard, J., Renard, F., Mittempergher, S., Doan, M.-L., Di Toro, G., Hadizadeh, J., Boullier, A.-M., 2011. Aseismic sliding of active faults by pressure solution creep: evidence from the San Andreas fault Observatory at depth. Geology 39, 1131–1134.

Gratier, J.-P., 2011. Fault Permeability and strength evolution related to fracturing and healing episodic processes (Years to Millennia): the Role of pressure solution. Oil Gas Sci. Technol. Rev. IFP Energies Nouvelles 66 (3), 491–506.

Heap, M.J., Faulkner, D.R., 2008. Quantifying the evolution of static elastic properties as crystalline rock approaches failure. Int. J. Rock Mech. Min. Sci. 45, 564–573.

Hild, F., Denoual, C., Forquin, P., Brajer, X., 2003a. On the probabilistic-deterministic transition involved in a fragmentation process of brittle material. Comp. Struct. 81, 1241–1253.

Hild, F., Forquin, P., Cordeiro da Silva, A.R., 2003b. Single and multiple fragmentation of brittle geomaterials. Rev. Fr. Génie Civil 7 (7–8), 973–1003.

Irwin, G., 1957. Analysis of stresses and strain near the end of a crack traversing a plate. Trans. ASME. Ser. E: J. Appl. Mech. 24 (3), 361–364.

Jayatilaka, A.de S., Trustrum, K., 1977. Statistical approach to brittle fracture. J. Mat. Sci. 12, 1426–1430.

Kolsky, H., 1963. Stress Waves in Solids. Dover Publications.

Mitchell, T.M., Ben-Zion, Y., Shimamoto, T., 2011. Pulverized fault rocks and damage asymmetry along the Arima-Takatsuki tectonic line, Japan: fault structure, damage distribution and textural characteristics. Earth Planet. Sci. Lett. 308 (3–4), 284–297.

Mitchell, T.M., Faulkner, D.R., 2009. The nature and origin of off-fault damage surrounding strike-slip fault zones with a wide range of displacements: a field study from the Atacama fault system, northern Chile. J. Struc. Geol. 31 (8), 802–816.

Nemat-Nasser, S., 2000. Mechanical Testing and Evaluation. In: ASM Handbook, vol. 8. ASM International, Ch. Introduction to high strain rate testing, pp. 427–428.

Paterson, M.S., Wong, T.-F., 2005. Experimental Rock Deformation – The Brittle Field, second ed. Springer.

Prentice, C.S., et al., 2009. Illuminating northern California's active faults. EOS Trans. Amer. Geophys. U 90 (7), 55.

Rockwell, T.K., Sisk, M., Girty, G., Dor, O., Wechsler, N., Ben-Zion, Y., 2009. Granulometric and mineralogical properties of pulverized rocks from Tejon pass on the San Andreas fault and from Tejon Ranch on the Garlock fault, California. Pure Appl. Geophys. 166 (10–11), 1725–1746.

Savage, H.M., Brodsky, E.E., 2011. Collateral damage: evolution with displacement of fracture distribution and secondary fault strands in fault damage zones. J. Geophys. Res. 116 (B3). doi:10.1029/2010JB007665

Shi, Z., Ben-Zion, Y., 2006. Dynamic rupture on a bimaterial interface governed by slip-weakening friction. Geophys. J. Int. 165, 469–484.

Vermilye, J.M., Scholz, C.H., 1998. The process zone: a microstructural view of fault growth. J. Geophys. Res. 103, 12223–12237.

Wechsler, N., Allen, E.E., Rockwell, T.K., Girty, G., Chester, J.S., Ben-Zion, Y., 2011. Characterization of pulverized granitoids in a shallow core along the San Andreas fault, little rock, CA. Geophys. J. Int. 186, 401–407.

Weibull, W., 1951. A statistical distribution function of wide applicability. J. Appl. Mech. – Trans. ASME 18, 293–297.

Wessel, P., Smith, W.H.F., 1998. Improved version of Generic Mapping Tools released. EOS Trans. Amer. Geophys. U 79 (47), 579.

Wilson, B., Dewers, T., Reches, Z., Brune, J., 2005. Particle size and energetics of gouge from earthquake rupture zones. Nature 434, 749–752.

Yuan, F., Prakash, V., Tullis, T., 2011. Origin of pulverized rocks during earthquake fault rupture. J. Geophys. Res. 116, B06309.